Available online at www.sciencedirect.com
SCIENCE DIRECT
International Journal of Heat and Fluid Flow 27 (2006) 490–501
International Journal of HEAT AND FLUID FLOW
www.elsevier.com/locate/ijhff

Transition from gravity- to inertia-dominated behavior computed for the turbulent stably-stratified filling of an open enclosure

Ying Ji, K.O. Homan *

Department of Mechanical and Aerospace Engineering, University of Missouri-Rolla, Rolla, MO 65409-0050, United States

Received 18 January 2005; accepted 25 November 2005
Available online 20 January 2006

Abstract

This paper treats the unsteady mixed convection processes occurring during the stably-stratified bottom filling of an open enclosure with application to stratified thermal storage devices. Central to the performance of these devices is the extent of thermal mixing which occurs at the interface between the hot and cold fluid volumes as one or the other is displaced from the vessel. Useful volume fraction, a parameter reflecting the temperature limited usefulness of the stored fluid, and internal entropy generation are used to characterize the extent of thermodynamic losses in time and their variation with flow rates ranging from well-stratified to highly-mixed conditions. The transition to highly-mixed behavior is critically important since it limits the achievable energy discharge rates. Distinct trends in the variation of cumulative performance with Reynolds number indicate this transition occurs at Froude numbers of approximately one and lead to identification of a gravity-dominated and an inertia-dominated regime. In the gravity-dominated regime, the useful volume fraction increases linearly with time after an initial adjustment period and the turbulent diffusivity affects the variation of entropy generation only at the edges of the relatively distinct thermocline. Within the thermocline, the turbulent kinetic energy is completely damped by gravity. However, in the inertia-dominated or highly-mixed regime, the useful volume fraction starts to drop in the later stages of the filling process and appreciable entropy generation levels are distributed across a relatively wide thermocline with turbulent diffusivity playing a significant role throughout.

Keywords: Thermal energy storage; Stratified flow; Mixed convection; Unsteady mixing

1. Introduction

Thermal energy storage provides a valuable means of storing heating or cooling capacity in applications for which there is a mismatch in timing or energy transfer rate between the energy supply and energy use. For modest temperature differences, stratified thermal storage is widely used due to its simplicity and cost-effectiveness. In these devices, buoyancy is the only mechanism separating the inflow fluid from the stored fluid during both the charging and discharging processes. The degree of internal mixing between the relatively high and low temperature fluids determines the ultimate performance of the storage device since the thermal mixing produces a blended volume suitable neither for cooling nor for heating and therefore decreases the true thermodynamic efficiency. Since the filling process involves displacement of stored fluid by a simultaneous inflow and withdrawal, the mixing process is intrinsically unsteady.

The behavior of stratified storage devices has attracted considerable research attention, both from an experimental and a numerical standpoint. Numerical models of stratified thermal storage have included simplified one-dimensional as well as two-dimensional descriptions, including both laminar and turbulent flows. One-dimensional models achieve agreement with experimental data only by incorporating some form of empirical correction (Cole and Bellinger, 1982; Han et al., 1978; Mavros et al., 1994; Oppel

* Corresponding author. Tel.: +1 573 341 6622; fax: +1 573 341 4115.
E-mail address: khoman@umr.edu (K.O. Homan).

0142-727X/$ - see front matter © 2006 Elsevier Inc. All rights reserved.
doi:10.1016/j.ijheatfluidflow.2005.11.006

Notation

Dimensional quantities are denoted by a hat, e.g. $\hat{t}$

A_c	cross-sectional area (dimensional)
c	specific heat
Ec_0	Eckert number, $\hat{u}_s^2/c\hat{T}_c$
Fr	inlet Froude number, $\hat{u}_s/\sqrt{g'\hat{h}_s}$
g	gravitational constant
g'	reduced gravity, $g\beta\Delta\hat{T}_s$
H	enclosure height (dimensional)
$\hat{h}_s$	inlet height
K	turbulent kinetic energy
k	thermal conductivity
L	enclosure length (dimensional)
m	maximum
Pe	Peclet number, $\hat{v}_b H/\alpha$
Pr	Prandtl number
p	pressure
Re	inlet Reynolds number, $\hat{u}_s\hat{h}_s/v$
S_g	cumulative entropy generation
$\dot{S}_g$	entropy generation rate
$\dot{S}'''_g$	volumetric entropy generation rate
T	temperature
t	time
$\Delta\hat{T}_s$	temperature difference scale
u, v	velocity components
$\hat{u}_s$	inlet velocity
V	volume (dimensional)
$\dot{V}$	volumetric flow rate (dimensional)
$\hat{v}_b$	bulk vertical velocity, $\dot{V}/A_c$
X	enclosure length
x, y	Cartesian coordinates
Y	enclosure height

Greeks

α	thermal diffusivity
β	thermal expansion coefficient
ε	turbulent dissipation
μ	viscosity
v	kinematic viscosity
ϕ	useful volume fraction
ρ	density
σ_t	turbulent Prandtl number
τ_c	temperature difference ratio, $\Delta\hat{T}_s/\hat{T}_c$

Subscripts and superscripts

a	horizontally averaged
b	bulk
c	cold
e	effective
f	filling
h	hot
i	inlet
k	thermal
μ	viscous
s	scale
t	turbulent

et al., 1986; Truman and Wildin, 1989; Zurigat et al., 1991). Without explicit empirical correction, a suitable numerical model must account for variations in at least two spatial dimensions, as well as in time. However, the application of multi-dimensional model predictions has typically been limited to qualitative assessments of temperature and velocity fields (Cabelli, 1977; Cai et al., 1993; Guo and Wu, 1985; Hahne and Chen, 1998; Mo and Miyatake, 1996; Spall, 1998). While certainly useful, a quantitative means of assessing the level of thermal mixing and its variation with key performance measures is crucial to the engineering application of these devices.

Quantitative comparison of the effects of physical and geometrical parameters on the complex behavior of stratified thermal storage is critically important. Quantitative measures based on thermocline thickness or cold volume fraction are of some value (Bahnfleth and Musser, 1999; Homan and Soo, 1998), but become less meaningful as the extent of thermal mixing increases and a distinct thermocline becomes less apparent. Even at high levels of thermal mixing, the fundamental issue remains loss of energy quality and entropy generation therefore provides a natural means to quantify the irreversibility of this transient mixing process, both on an instantaneous and on a cumulative basis. For multi-dimensional flows, minimizing entropy generation by analyzing local sources of irreversibility has been applied to several basic heat transfer configurations (Benedetti and Sciubba, 1993; Cheng and Huang, 1989; Cheng et al., 1994; Drost and White, 1991). However, there is no existing analysis of local entropy generation in stratified thermal storage for multi-dimensional flow, except at relatively low Reynolds numbers (Homan, 1999).

The second law of thermodynamics was first introduced into the analysis of sensible thermal storage by Bejan (1978) in his analysis of indirect systems with a single fully-mixed storage element. In the indirect configuration, energy transfers to and from the storage component cross either a phase or a material interface, such as in gas–solid and fluid–fluid systems, respectively. Since then, numerous investigations have focused on minimizing entropy generation for the indirect configuration (Bejan, 1978, 1996; Krane, 1987; Krane and Krane, 1992a,b; Moran and Keyhani, 1982), although for fluid–fluid systems, the temperature field has been taken to be spatially uniform at every instant in time. For the direct configuration, in which energy transfers to and from the storage component are accomplished by displacement of the stored fluid, Homan (2003) provided analytical results for the entropy

generation of the fully-mixed and ideally-stratified limits which, in practical terms, correspond to relatively high and low system flow rates, respectively. Although these two limits provide practical bounds for the entropy generation in direct thermal storage, the nature of the transition between these two limits has not been established.

In the present work, a two-dimensional buoyant K–ε model has been utilized to simulate the stably-stratified bottom filling of an open vessel. Useful volume fraction and local entropy generation are computed for a practically important range of inlet Reynolds numbers and temperature difference ratios. The observed variation of these two performance measures leads to identification of the transition from well-stratified to highly-mixed condition and a division between gravity-dominated and inertia-dominated regimes. A thermal mixing factor, based on the useful volume fraction, is utilized to characterize the level of mixing. The computed entropy generation is examined with respect to the fully-mixed and ideally-stratified limits and used to identify key sources of irreversibility occurring during the transient charging process.

2. Problem formulation

The domain of interest, shown in Fig. 1, is a rectangular enclosure with a dimensional length and height of L and H, respectively, and a dimensional inlet and outlet height of $\hat{h}_s$. During the charging process, cold water at a uniform temperature $\hat{T}_c$ and a uniform velocity $\hat{u}_s$ enters the vessel which is initially filled with hotter water at a uniform temperature $\hat{T}_h$. Water leaves the vessel through an outlet slot at a rate identical to that at which it enters through the inlet slot.

2.1. Unsteady transport equations

The transient filling process is modeled by a two-dimensional high Reynolds number K–ε model assuming the inlet velocity is uniform and the length of the inlet slot is wide enough to neglect the effect of the side wall on the flow field. The numerical model consists of equations for time-averaged continuity, momentum, thermal energy, turbulent kinetic energy, and dissipation rate of turbulent kinetic energy. In the momentum equation, the Boussinesq assumption is employed to account for the buoyancy effects due to temperature difference. The governing equations are non-dimensionalized by taking the inlet height, $\hat{h}_s$, as the length scale, and the inlet velocity, $\hat{u}_s$, as the velocity scale. The local time scale is therefore $\hat{h}_s/\hat{u}_s$. Upon substitution of these scales, the continuity and momentum equations take the form:

$$\frac{\partial u_j}{\partial x_j} = 0 \tag{1}$$

and

$$\frac{\mathrm{D}u_i}{\mathrm{D}t} = -\frac{\partial p}{\partial x_i} + \frac{\delta_{i2}}{Fr^2}T + \frac{1}{Re}\frac{\partial}{\partial x_j}\left\{\left(1+\frac{\nu_t}{\nu}\right)\left(\frac{\partial u_i}{\partial x_j}+\frac{\partial u_j}{\partial x_i}\right)\right\}, \tag{2}$$

where the dimensionless pressure is defined as $p \equiv (\hat{p}-\hat{p}_i)/(\rho\hat{u}_s^2)$ and the dimensionless temperature as $T \equiv (\hat{T}-\hat{T}_c)/\Delta\hat{T}_s$, along with $Re \equiv \hat{u}_s\hat{h}_s/\nu$, and $Fr^2 = \hat{u}_s^2/(g\beta\Delta\hat{T}_s\hat{h}_s)$. The Kronecker delta, δ_{ij}, has the usual meaning and $\mathrm{D}/\mathrm{D}t$ denotes the substantial derivative.

In dimensionless form, the thermal energy equation is

$$\frac{\mathrm{D}T}{\mathrm{D}t} = \frac{1}{RePr}\frac{\partial}{\partial x_j}\left\{\left(1+\frac{(\nu_t/\nu)Pr}{\sigma_t}\right)\frac{\partial T}{\partial x_j}\right\}, \tag{3}$$

where σ_t is the turbulent Prandtl number. The turbulent kinetic energy and dissipation equations (Rodi, 1979) are then

$$\frac{\mathrm{D}K}{\mathrm{D}t} = \frac{1}{Re}\frac{\partial}{\partial x_j}\left\{\left(1+\frac{\nu_t/\nu}{\sigma_K}\right)\frac{\partial K}{\partial x_j}\right\} + P + G - \varepsilon \tag{4}$$

and

$$\frac{\mathrm{D}\varepsilon}{\mathrm{D}t} = \frac{1}{Re}\frac{\partial}{\partial x_j}\left\{\left(1+\frac{\nu_t/\nu}{\sigma_\varepsilon}\right)\frac{\partial \varepsilon}{\partial x_j}\right\} + \{c_1(P+G-c_3G)-c_2\varepsilon\}\frac{\varepsilon}{K}, \tag{5}$$

where the dimensionless turbulent kinetic energy is defined as $K \equiv \hat{K}/\hat{u}_s^2$, the dimensionless turbulent dissipation as $\varepsilon \equiv \hat{\varepsilon}/(\hat{u}_s^3/\hat{h}_s)$, and both σ_K and σ_ε are model coefficients. The dimensionless shear production P, buoyant production G, and the turbulent kinematic viscosity ν_t are, in turn, defined as

$$P \equiv \frac{\hat{P}}{\hat{u}_s^3/\hat{h}_s} = \frac{\nu_t/\nu}{Re}\left(\frac{\partial u_i}{\partial x_j}+\frac{\partial u_j}{\partial x_i}\right)\frac{\partial u_i}{\partial x_j}, \tag{6}$$

$$G \equiv \frac{\hat{G}}{\hat{u}_s^3/\hat{h}_s} = -\frac{\nu_t/\nu}{\sigma_t Re\, Fr^2}\delta_{j2}\frac{\partial T}{\partial x_j}, \tag{7}$$

and

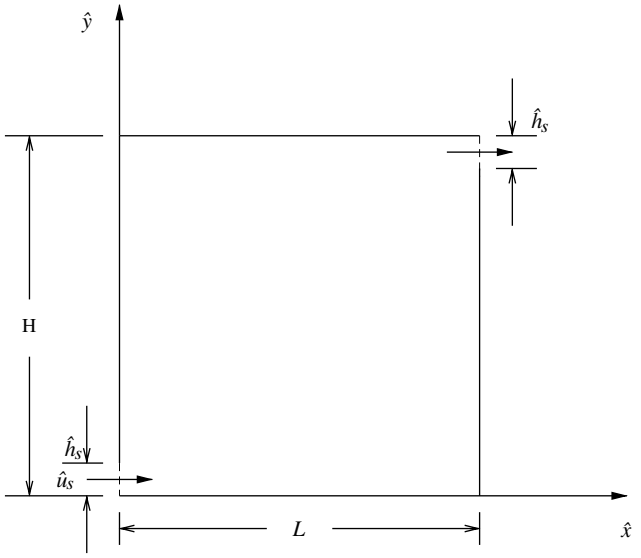

Fig. 1. Schematic of enclosure with a single inlet and outlet.

$$\frac{v_t}{v} = c_D Re \frac{K^2}{\varepsilon}. \quad (8)$$

The values of the constants appearing in the equations are: $c_D = 0.09$, $c_1 = 1.44$, c_2=1.92, $c_3 = 0.80$, $\sigma_t = 1.0$, $\sigma_K = 1.0$, and $\sigma_\varepsilon = 1.30$ (Mo and Miyatake, 1996; Nakayama, 1995; Rodi, 1979; White, 1991).

The K–ε model adopted in the present study is a linear model. Although higher-order (non-linear) models have been developed, such as by Speziale (1987) and Craft et al. (1996), they exhibit significant merit in circumstances for which normal stresses are of central importance. However, in the physical configuration considered in the present study, the dominant stresses are the Reynolds shear stresses at the interfacial layer. These are the stress components which linear models have been shown to accurately predict. The linear model adopted in the present study is consistent with long-standing recommendations for the modeling of horizontal shear flows (Rodi, 1979). Further, investigations of pollutant transport dynamics using a linear K–ε model in a similar physical configuration have shown suitable agreement with experiments (Lage et al., 1991, 1992). The buoyancy production term in the turbulent dissipation equation is of the form recommended by Rodi (1979) for buoyant shear layers.

2.2. Boundary and initial conditions

Adiabatic and no-slip boundary conditions are applied along each of the solid boundaries shown in Fig. 1. Along these boundaries, K and ε are set to 10^{-15}. The boundary conditions applied at the inlet are a uniform horizontal velocity $\hat{\mu}_s$ and uniform temperature $\hat{T}_c$ along with small values of the turbulent kinetic energy and dissipation. In dimensionless terms, $u = 1$, $v = 0$, $T = 0$, and $K = \varepsilon = 10^{-15}$. At the exit, a zero gradient condition is applied for each of the dependent variables u, v, T, K, and ε. Along the fixed upper surface, a slip condition is applied in which $v = 0$ and the vertical gradient in all other variables (u, K, ε, and T) is set to zero.

The initial condition for the filling process is a fluid at rest with a uniform temperature $\hat{T}_h$. In dimensionless form, $u = 0$, $v = 0$, and $T = 1$. The dimensionless turbulent kinetic energy and dissipation are initialized to small values, $K = 1.6 \times 10^{-3}$ and $\varepsilon = 2.56 \times 10^{-4}$.

2.3. Solution method

A staggered grid system is adopted in which the velocities are defined on the faces of the control volumes and are therefore staggered with respect to p, T, K, and ε. Since thermal transport is central to the stratification process, a higher-order convective scheme is necessary to solve the energy equation with minimal numerical diffusion. The QUICKEST (QUICK with estimated streaming part) scheme, originally proposed by Leonard (1979), has been applied in the thermal energy equation and has third order accuracy in time and space. In the other transport equations, an implicit hybrid differencing scheme is used (Patankar, 1980). Our results have shown that when the energy equation is solved by a hybrid scheme, the thermocline thicknesses are physically unrealistic. However, when the QUICKEST scheme is utilized in the energy equation, thermocline thicknesses are of the scale observed experimentally. The set of coupled equations are solved by the SIMPLE (Semi-Implicit Pressure Linked Equation) algorithm originally proposed by Patankar (1980). A uniform grid has been used throughout the computational domain, since the thermocline is transported through the entire domain and adequate resolution must therefore be maintained throughout the filling process. Within each time step, the pressure iteration is stopped when the mass residual is less than 10^{-3}.

2.4. Useful volume fraction

One way of indirectly measuring the thermal mixing is to compute the accumulation of fluid in the storage vessel at or below a maximum temperature for cool storage applications. This has been termed the cold volume or the useful volume fraction when expressed relative to the volume of the storage vessel (Homan and Soo, 1998). For the two-dimensional model, the useful volume fraction at any time of the filling process is computed from

$$\phi \equiv \frac{1}{XY}\frac{\hat{\phi}}{\hat{h}_s^2} = \frac{1}{XY}\int_0^Y \int_0^X \mathscr{H}[T_m - T(x,y,t)]\,dx\,dy, \quad (9)$$

where T_m corresponds physically to the maximum useful temperature for the discharging process and the Heaviside function $\mathscr{H}$ is defined as

$$\mathscr{H}[T_m - T(x,y,t)] \equiv \begin{cases} 0 & T(x,y,t) \geqslant T_m, \\ 1 & T(x,y,t) < T_m. \end{cases} \quad (10)$$

Numerically, the integral appearing in Eq. (9) is evaluated by using the trapezoidal rule. An obvious point of comparison for the useful volume fraction is the cumulative amount of cold fluid put into the tank,

$$\phi_i(t) \equiv \frac{1}{XY}\frac{\hat{\phi}_i}{\hat{h}_s^2} = \frac{1}{XY}\int_0^t dt \int_0^1 u(0,y,t)\mathscr{H}[T_m - T(0,y,t)]\,dy. \quad (11)$$

For uniform inlet velocity and temperature, $\phi_i(t) = t$.

2.5. Local entropy generation

The volumetric entropy generation rate in a laminar flow (Bejan, 1996; Bird et al., 1960) is given by

$$\hat{S}_g''' = \frac{k}{\hat{T}^2}(\hat{\nabla}\hat{T})^2 + \frac{\mu}{\hat{T}}\hat{\Phi}, \quad (12)$$

whereas, in a turbulent flow, the transport coefficients are modified to include the turbulent contribution,

$$\hat{\dot{S}}_g''' = \frac{k + k_t}{\hat{T}^2}(\hat{\nabla}\hat{T})^2 + \frac{\mu + \mu_t}{\hat{T}}\hat{\Phi} \tag{13}$$

in which $\hat{T}$ is the dimensional Reynolds-averaged temperature (Drost and White, 1991). Recognizing the first term in Eq. (13) as reflecting the entropy generation due to thermal diffusion and the second due to viscous dissipation, the total volumetric entropy generation rate can be expressed as

$$\hat{\dot{S}}_g''' = \hat{\dot{S}}_{g,k}''' + \hat{\dot{S}}_{g,\mu}''', \tag{14}$$

where the subscript k and μ are used to indicate the effects of thermal diffusion and viscous dissipation, respectively.

Introducing $\rho c\dot{V}$ as the scale for $\hat{\dot{S}}_g$ along with the previously identified length, velocity, and temperature scales, the dimensionless two-dimensional generation rate simplifies to

$$\dot{S}_g'' = \frac{\tau_c^2}{Re\,Pr}\left(1 + \frac{k_t}{k}\right)\left(\frac{\nabla T}{1 + \tau_c T}\right)^2 + \frac{Ec_0}{Re}\left(1 + \frac{\mu_t}{\mu}\right)\frac{\Phi}{1 + \tau_c T}, \tag{15}$$

where $\tau_c \equiv \Delta\hat{T}_s/\hat{T}_c$ and $Ec_0 \equiv \hat{u}_s^2/(c\hat{T}_c)$. The total entropy generation rate is then given by

$$\dot{S}_g(t) = \int_0^X \int_0^Y \dot{S}_g''\,dx\,dy \tag{16}$$

and the cumulative entropy generation by

$$S_g = \frac{1}{XY}\int_0^{t_f} \dot{S}_g\,dt, \tag{17}$$

where $S_g \equiv \hat{S}_g/\rho cV$, $X \equiv L/\hat{h}_s$ and $Y \equiv H/\hat{h}_s$. The choice of enclosure-level scales for $\hat{\dot{S}}_g$ and $\hat{S}_g$ rather than inlet scales is intentional as it will simplify comparison with corresponding quantities from more simplified transport models. The ratio of turbulent thermal conductivity to molecular thermal conductivity can be related to the ratio of turbulent kinematic viscosity to kinematic viscosity by

$$\frac{k_t}{k} = \frac{\mu_t c/\sigma_t}{\mu c/Pr} = \frac{Pr}{\sigma_t}\frac{\mu_t}{\mu}, \tag{18}$$

where μ_t/μ is identically equal to ν_t/ν, as given earlier.

2.6. Grid resolution

The effects of grid resolution have been examined by considering several levels of grid resolution for the modeling of the cold water charging process. The results show a relatively small difference between employing a 160 by 160 versus 200 by 200 grid. For example, when $Re = 5\times10^3$ and $\tau_c = 0.05$, there is only a 7% difference in the cumulative entropy generation and only a 2% difference in the useful volume fraction when one vessel volume of cold water has passed through the inlet. Since the entropy generation is computed from local temperature and velocity gradients, it provides a particularly sensitive indication of grid resolution. Due to the vastly larger computing time required for the finer grid, a 160 by 160 grid was utilized throughout the present investigation. This level of grid resolution is consistent with previously published results based on the K–ε model for similar problems (Chen, 1995; Mo and Miyatake, 1996; Spall, 1998). In addition, the computed results asymptote to the analytically-derived limits of the ideally-stratified and fully-mixed behaviors which provide further indication of the accuracy in the entropy generation calculation.

3. Results and discussion

The described numerical model simulates the cold water bottom filling of a two-dimensional rectangular vessel initially containing hot water at uniform temperature. In the present paper, the two-dimensional computational domain is held fixed at $X = Y$, and the dimensionless values of X and Y are selected as 20. In chilled water storage applications, the aspect ratio Y/X typically varies from 0.5 to 1.2 and the ratio of the enclosure height to inlet height in the range of 10–20 (Dorgan and Elleson, 1994). The temperature difference ratio, τ_c, is varied over the range 0.02–0.075 which is representative of cool storage applications. The selected values of τ_c correspond to temperature differences of approximately 3–25 °C with a cold inlet temperature of approximately 5 °C. Cases were computed for inlet Reynolds numbers of 5×10^3 to 1×10^5. Twenty five separate cases were generated by combining five values for Re and τ_c. With $\hat{T}_c$ held constant, the temperature difference ratio and Froude number are not independent. Since the Froude number is an established parameter for description of the initial stages of the filling process, the selected Froude number values for different Re and τ_c combinations are shown in Table 1 along with the corresponding Prandtl numbers for each of the different temperature difference ratios. The Prandtl number is evaluated at the average of the cold and hot water temperatures.

Based on the present choice of length and time scale, the dimensionless time required to fill the vessel is the same, that is, $t_f = XY = 400$. For convenience of interpretation, a dimensionless filling time, t^*, is introduced according to

$$t^* = \frac{t}{t_f}. \tag{19}$$

Thus, t^* is identically equal to one when a single enclosure volume of fluid has passed through the vessel.

Table 1
Inlet Froude and Prandtl numbers corresponding to the selected Re and τ_c cases

Re	τ_c				
	0.01	0.03	0.05	0.07	0.09
5.0e3	0.57	0.24	0.16	0.11	0.09
1.0e4	1.14	0.49	0.33	0.23	0.18
2.0e4	2.29	0.98	0.66	0.45	0.36
5.0e4	5.72	2.44	1.64	1.13	0.90
1.0e5	11.43	4.87	3.29	2.27	1.80
Pr	10.20	9.33	8.56	7.87	7.27

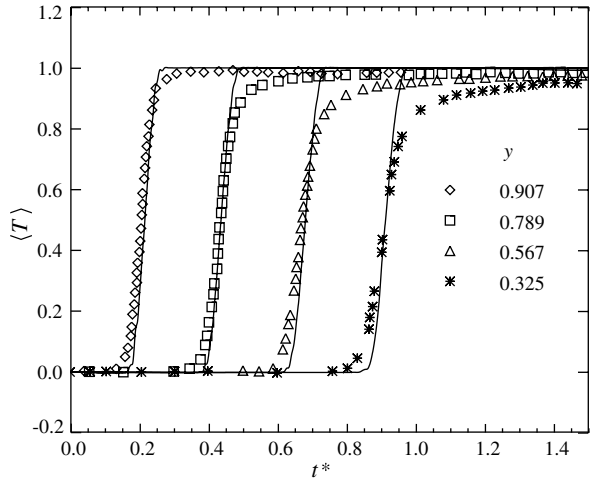

Fig. 2. Comparison of area-averaged temperature traces, $\langle T\rangle$, at several vertical positions during the cold water discharging process for $Re = 5000$ and $Fr = 0.80$. Curves and symbols represent numerical and experimental data, respectively.

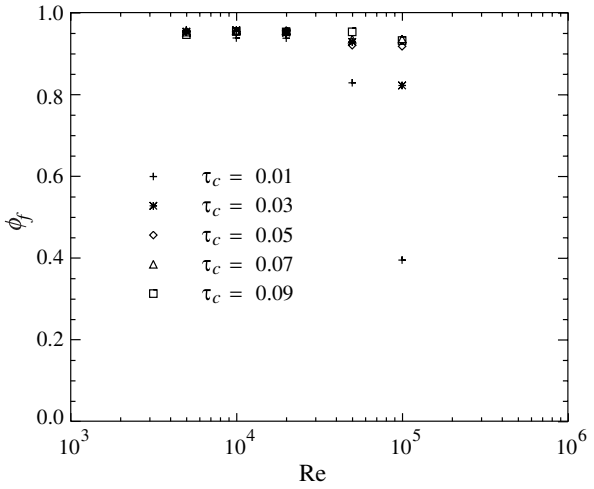

Fig. 3. Useful volume fraction versus Reynolds number for the duration of the filling process, $t^* = 1$. The maximum useful temperature is taken as $T_m = 0.10$.

The numerical simulation has been validated by comparison to existing experimental data taken during the stably-stratified top filling of an open enclosure (Mo and Miyatake, 1996). A comparison of horizontally-averaged temperature traces, denoted by $\langle T\rangle$, at four vertical locations for numerical and experimental data are shown in Fig. 2 at several instants during the cold water discharging process for $Re = 5000$ and $Fr = 0.80$. Although some discrepancies between the numerical and experimental data are evident, particularly where the temperature approaches 1.0 on the inlet side of the thermocline, the numerical model predicts the evolution of the gradient layer reasonably well.

3.1. Cumulative performance

The useful volume fraction versus Reynolds number at $t^* = 1$ is shown in Fig. 3. For Reynolds number smaller than approximately 2×10^4, the useful volume fractions are almost the same for different Reynolds numbers and the temperature difference ratio has only a minor impact. As Reynolds number increases, the useful volume fraction decreases rapidly, especially for lower temperature difference ratios. For example, with $Re = 1 \times 10^5$ and $\tau_c = 0.01$, the useful volume fraction drops to about 0.4.

A thermal mixing factor, κ, may be defined in terms of the useful volume fraction by

$$\kappa \equiv 1 + \frac{\alpha_e}{\alpha} = \frac{Pe}{4t^*}\left(\frac{t^* - \phi}{a}\right)^2, \tag{20}$$

where a is a constant depending upon T_m and α_e is the effective thermal diffusivity based on a uniform thermal diffusivity across the advected thermal interface (Homan and Soo, 1998). The Peclet number is related to the Reynolds number and Prandtl numbers by

$$Pe = RePr\left(\frac{H}{L}\right) = RePr \tag{21}$$

since, in the present paper, the height and length of the enclosure are identical. The thermal mixing factor versus $Fr^2\,Pe$ at the filling time of 1.0 is shown in Fig. 4.

The thermal mixing factor appears to be nearly constant when $Fr^2\,Pe$ is less than 10^4 and then begins to increase relatively rapidly. Note that with use of $Fr^2\,Pe$ as the abscissa, the variation of the thermal mixing factor collapses to a single curve for all temperature difference ratios since decreasing τ_c corresponds to increasing Fr.

Although useful volume fraction and thermal mixing factor provide useful engineering information about the quality of the stored fluid and the level of thermal mixing, respectively, the spatial distribution of losses due to thermal mixing cannot be determined from these parameters.

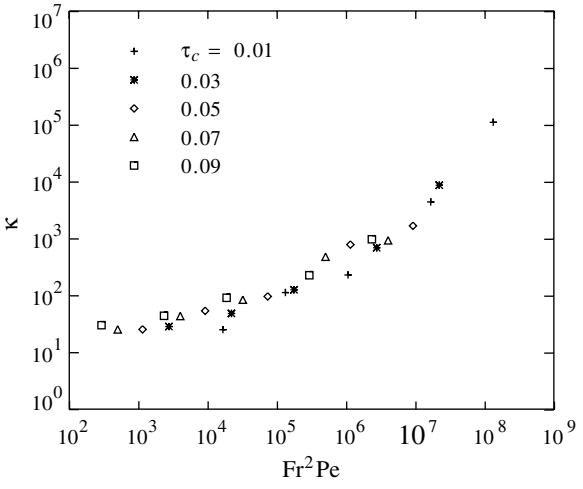

Fig. 4. Thermal mixing factor versus $Fr^2\,Pe$ for the duration of the filling process, $t^* = 1$. The maximum useful temperature is held fixed at $T_m = 0.10$.

Entropy generation, however, allows one to quantify both the temporal and spatial variation of losses due to thermal mixing. The variation of the cumulative entropy generation with Reynolds numbers is shown in Fig. 5(a). At a fixed Reynolds number, the cumulative entropy generation increases with τ_c except for $Re = 2 \times 10^4$ at $\tau_c = 0.03$ and $\tau_c = 0.05$. This reflects the fact that although the stabilizing effect of gravity increases with τ_c, the entropy generation generally increases more rapidly since the heat transfer is occurring across a larger overall temperature difference. Alternatively, holding the temperature difference ratio fixed, the cumulative entropy generation remains essentially constant at lower Reynolds numbers. The extent of this range increases with the temperature difference ratio. For example, at $\tau_c = 0.03$, the cumulative entropy generation $S_{g,f}$ is nearly constant for Reynolds numbers less than 1×10^4 whereas for $\tau_c = 0.09$, the dimensionless entropy generation is nearly constant to $Re = 5 \times 10^4$. For Reynolds numbers above this range, the cumulative entropy generation increases at approximately the same rate for all of the temperature difference ratios examined.

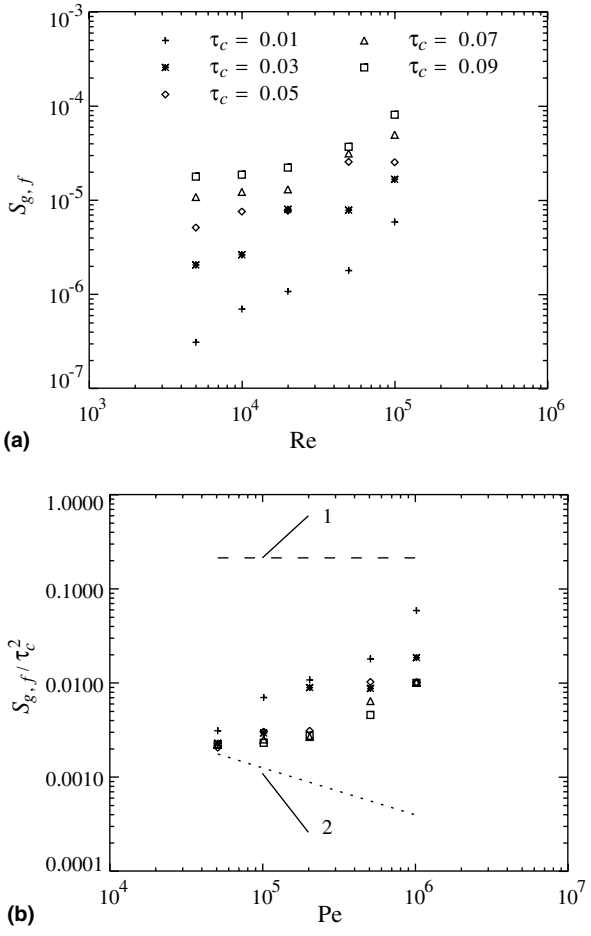

Fig. 5. Cumulative entropy generation versus Reynolds number and versus Peclet number for the duration of the filling process, $t^* = 1$. The plot symbols have identical meaning in both subfigures. Theoretical limits are the fully-mixed and ideally-stratified behaviors, denoted by curves 1 and 2, respectively.

Dividing the cumulative entropy generation by the square of the temperature difference ratio facilitates comparison with the analytic fully-mixed and ideally-stratified limits (Homan, 2003). In the fully-mixed limit, the temperature field is spatially uniform at every instant of the filling process, hence $T = T(t)$. In the ideally-stratified limit, the only thermal contact between the hot and cold water volumes is by molecular diffusion across a planar interface, hence $T = T(t, y)$. In the fully-mixed limit, the cumulative entropy generation divided by the square of τ_c is constant to leading order. In contrast, the cumulative entropy generation divided by τ_c^2 in the ideally-stratified limit varies inversely with $\sqrt{Pe}$. The cumulative entropy generation divided by the square of the temperature difference ratio as computed from the present numerical model is shown in Fig. 5(b) versus Peclet number. Higher order terms in the relation between S_g and τ_c for the fully-mixed limit have not been included and differences in the Peclet number due to variations in the Prandtl number have been ignored for the ideally-stratified limit. In each of these two limits, these higher order contributions are of vanishing significance. The cumulative entropy generation computed from the present model is well bounded by these two limits. As Peclet number increases, the entropy generation computed from the present results trends toward the fully-mixed limit and as expected, larger temperature difference ratios trend closer to the ideally-stratified limit reflecting a stronger stabilizing effect of gravity.

The Reynolds number of the transition point from $S_{g,f}$ being constant with Re to increasing with Re clearly changes with the temperature difference ratio. However, all of the transition points lie at an inlet Froude number of about 1.0. This provides further reinforcement for the general guideline that the inlet Froude number should be less than 1.0 in order to maintain desirable stratification, as originally noted by (Yoo et al., 1986). Interestingly, Yoo et al. (1986) based their recommendation on largely visual observations of the *initial* passage of the inflow gravity current. The present results suggest, however, that an order one Froude number provides an even more general criteria with consequence for the overall filling process. Recognizing the distinct variations with Reynolds number and to aid further analysis, the two behaviors are hereafter termed the gravity- and inertia-dominated regimes, corresponding to inlet Froude numbers less than and larger than unity, respectively. The two distinct regimes with unique characteristics provides a natural division for more detailed consideration of transients in the useful volume fraction and entropy generation rate. The remaining subsections therefore examine, in turn, the predicted transients in the gravity-dominated and inertia-dominated regimes.

3.2. Gravity-dominated regime

In the gravity-dominated regime, buoyancy is dominant and therefore provides a strongly stabilizing effect upon thermocline formation. The time variation of useful vol-

ume fraction during the charging process for a gravity-dominated case, $Re = 5 \times 10^3$, is shown in Fig. 6.

The useful volume fraction increases with time at a rate almost equal to unity except for the early stage of charging process. Apart from the initial stage of the filling processes, the rate of change of the useful volume fraction, ϕ, is essentially the same for all of the temperature difference ratios. Interestingly, the lower temperature difference ratios produce a higher useful volume fraction since the relatively higher level of thermal mixing in the gravity-dominated regime actually increases the useful volume fraction.

The entropy generation rate for a gravity-dominated case, $Re = 5 \times 10^3$, is shown in Fig. 7. The entropy generation rate is bounded by the fully-mixed limit during the whole charging process and is smaller than the ideally-stratified limit except for in the early and late stages of the charging process. The entropy generation rate increases to its peak value during the early stage of the charging process and then drops quickly to relatively stable values. The very high initial values for $\tau_c \geqslant 0.03$ are attributed to the step change in the inlet boundary condition which begins the filling process. The early peak in entropy generation is due to the mixing of the relatively cold inflow with the hot fluid initially in the tank. Once a stable thermocline has formed, the entropy generation rate becomes relatively constant. An entropy generation rate which peaks early in the charging process and then decreases to a relatively stable value coincides with previously published results for laminar flow at a Reynolds number of order 10^2 (Homan, 1999). For the Reynolds numbers examined, the late time values of entropy generation rate are smaller than the corresponding ideally-stratified values since a relatively thicker thermocline emerges from the initial mixing process. Finally, as the filling time approaches unity, the interaction of the thermocline with the outlet causes the entropy generation rate to once again increase. At very small times,

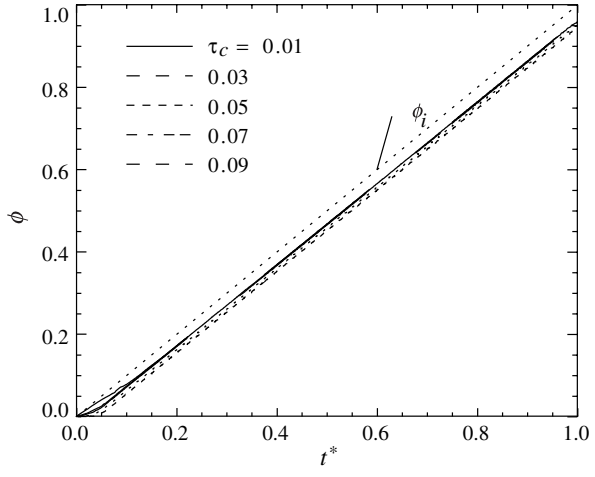

Fig. 6. Variation of useful volume fraction in time for $Re = 5 \times 10^3$ with a fixed $T_m = 0.10$.

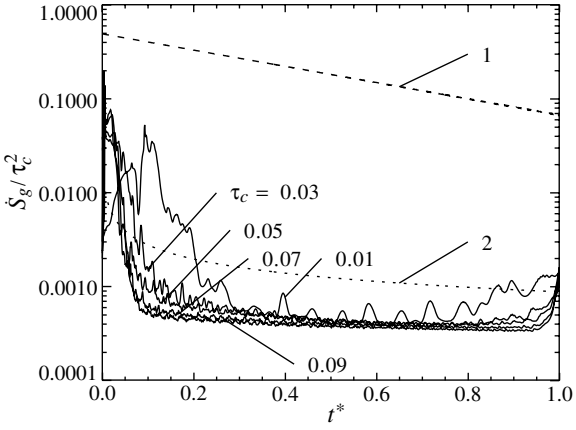

Fig. 7. Unsteady entropy generation rate for $Re = 5 \times 10^3$. Theoretical limits are the fully-mixed and ideally-stratified behaviors, denoted by curves 1 and 2, respectively.

the ideally-stratified limit also exhibits very high values of entropy generation due to the step change in the boundary condition (Homan, 2000).

The peak value in the entropy generation rate occurs at different times for different temperature difference ratios, as shown in Fig. 7.

For example, with $\tau_c = 0.01$, $\dot{S}_g/\tau_c^2$ has its peak value at $t = 37.2$ whereas for $\tau_c = 0.09$, $\dot{S}_g/\tau_c^2$ has its peak value at $t = 7.2$. Isotherm contours overlayed with instantaneous streamlines for these two times are shown in Fig. 8.

In both cases, the thermocline thickness is about 1/20th of the tank height at this stage of the charging process. At higher temperature difference ratios, the thermocline is thinner. The peak value for $\tau_c = 0.01$ occurs when the gravity current is bounced back by the wall opposite the inlet. In contrast, for $\tau_c = 0.09$, the peak value is attained just before the gravity current hits the wall opposite the inlet. In general, the peak of the entropy generation rate is therefore occurring during the process of initial thermocline formation.

The dimensional scale for the entropy generation rate, $\hat{\dot{S}}_g$, has been taken as $\rho c \dot{V}$ and therefore scales with Reynolds number. If the dimensional entropy generation rate is instead scaled by a local scale such as $k\hat{h}_s$, the entropy generation rate can be compared on an absolute basis. In the present formulation, this change of scale simplifies to multiplication of the dimensionless entropy generation rate by the $Re\,Pr$ product. As mentioned earlier, the entropy generation rate is composed of two components: the one caused by thermal diffusion and the other one caused by viscous dissipation. The relative magnitudes of the two components of entropy generation rate for $\tau_c = 0.01$ at several charging times are shown in Table 2.

As might be expected, entropy generation rates due to both thermal diffusion and viscous dissipation increase with inlet Reynolds number. The thermal entropy generation is between one and four orders of magnitude larger than the viscous entropy generation throughout the charging process.

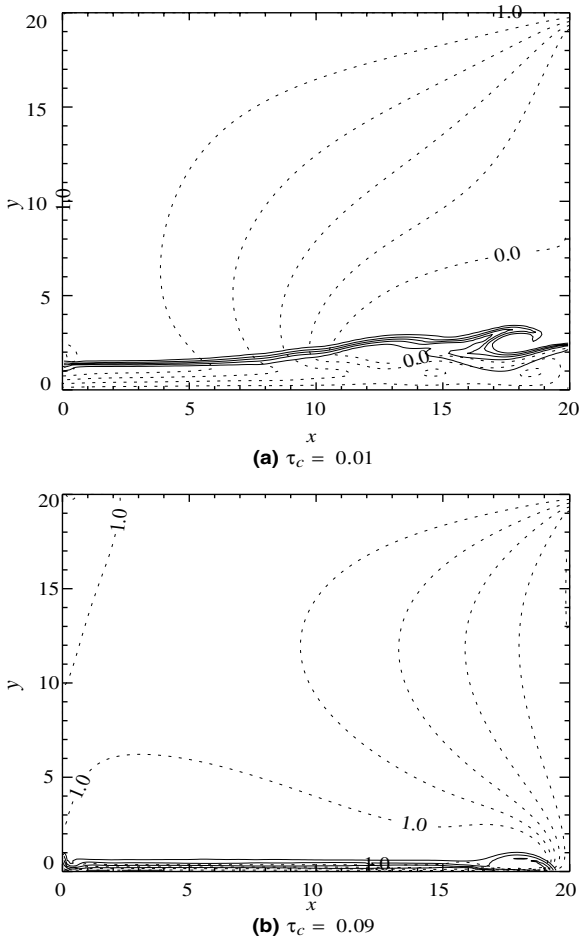

Fig. 8. Isotherm contours ($T = 0.1$, 0.3, 0.5, 0.7, and 0.9) overlayed with instantaneous streamlines ($\Delta\psi = 0.2$) for $Re = 5 \times 10^3$ at the instant $\dot{S}_g$ attains its peak value for select τ_c. For $\tau_c = 0.01$, $\dot{S}_g$ is maximum at $t = 37.2$, whereas for $\tau_c = 0.09$, $\dot{S}_g$ is maximum at $t = 7.2$.

An overlay of area-averaged temperature and the area-averaged K^2/ε ratio, denoted by $\langle T\rangle$ and $\langle K^2/\varepsilon\rangle$, is shown in Fig. 9 along with $\dot{S}'_g$ for $Re = 5 \times 10^3$ and $\tau_c = 0.05$. The area-averaged vertical temperature profiles reveal a sharp gradient layer between the cold and hot water due to relatively small mixing effects. The area-integrated entropy generation rate, $\dot{S}'_g$, is concentrated in the gradient layer region and shows the same basic variation at several times. The peak in $\dot{S}'_g$ coincides with the peak in the temperature gradient so that as the temperature gradient decreases, $\dot{S}'_g$ decreases. However, $\dot{S}'_g$ has a second peak

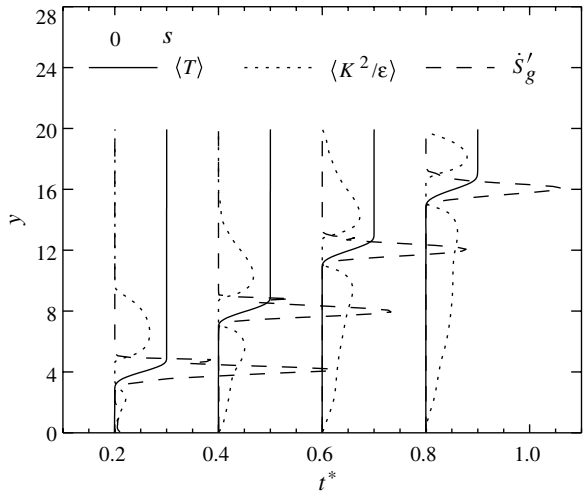

Fig. 9. Vertical profiles of area-averaged temperature, $\langle T\rangle$, ratio of turbulent kinetic energy to dissipation, $\langle K^2/\varepsilon\rangle$, and entropy generation rate, $\dot{S}'_g$ for $Re = 5 \times 10^3$ and $\tau_c = 0.05$. The scales are $s = 1.0$ for $\langle T\rangle$, $s = 1.0$ for $\langle K^2/\varepsilon\rangle$, and $s = 2.0 \times 10^{-8}$ for $\dot{S}'_g$.

at the top edge of the gradient layer. As previously observed, thermal effects dominate the entropy generation which leads to a concentration of $\dot{S}'_g$ in the thermal gradient layer. However, as seen from Eq. (15), the thermal entropy generation reflects both molecular diffusion and turbulent diffusion. Since the turbulent diffusion is proportional to

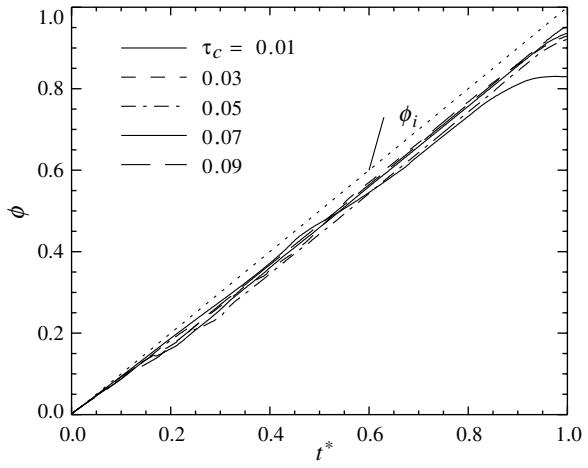

Fig. 10. Variation of useful volume fraction for $Re = 5 \times 10^4$ with a fixed $T_m = 0.10$.

Table 2
Components of entropy generation rate for $\tau_c = 0.01$

Re	$t = 10$		$t = 200$		$t = 390$	
	$RePr\dot{S}_{g,k}$	$RePr\dot{S}_{g,\mu}$	$RePr\dot{S}_{g,k}$	$RePr\dot{S}_{g,\mu}$	$RePr\dot{S}_{g,k}$	$RePr\dot{S}_{g,\mu}$
5.0e3	3.84e−2	2.25e−6	1.97e−3	3.61e−5	6.60e−3	2.71e−5
1.0e4	5.22e−2	8.16e−6	9.27e−3	2.72e−4	1.12e−2	2.35e−4
2.0e4	1.28e−1	3.61e−5	5.12e−2	2.55e−3	3.94e−1	2.33e−3
5.0e4	3.75e−1	4.62e−4	9.95e−1	2.65e−2	3.52e0	4.13e−2
1.0e5	7.72e−1	3.45e−3	6.89e0	1.39e−1	1.72e1	4.04e−1

K^2/ε, according to Eqs. (18) and (8), $\dot{S}'_g$ exhibits a second peak at the edge of the thermal gradient layer where turbulent diffusivity reaches appreciable levels. The turbulent viscosity increases from zero to a peak value below the thermocline and then decreases to zero at the bottom edge of the gradient layer. Within the thermal gradient layer, the turbulent kinetic energy is very small due to the stabilizing effect of gravity. Near the upper edge of the thermal gradient layer, it increases again, causing the second peak in $\dot{S}'_g$. Above this, the temperature gradient vanishes and $\dot{S}'_g$ therefore decreases to zero even though $\langle K^2/\varepsilon \rangle$ continues to increase.

3.3. Inertia-dominated regime

In the inertia-dominated regime, gravity plays a diminishing role, thereby allowing even greater levels of mixing between the cold water inflow and hot water initially in the enclosure. The time variation of useful volume fraction during the charging process for an inertia-dominated case, $Re = 5 \times 10^4$, is shown in Fig. 10.

At early stages of the charging process, all of the temperature difference ratios have a nearly identical variation in the useful volume fraction. Initially, a lower temperature difference ratio leads to higher useful volume fractions since the mixing increases the useful volume. Later, however, the useful volume fraction decreases rapidly for lower temperature difference ratios since the greater extent of mixing is producing a more uniform temperature field in which less volume satisfies the $T \leqslant T_m$ criterion.

The entropy generation rate for $Re = 5 \times 10^4$ is shown in Fig. 11. The cases with $\tau_c \leqslant 0.07$ belong to the

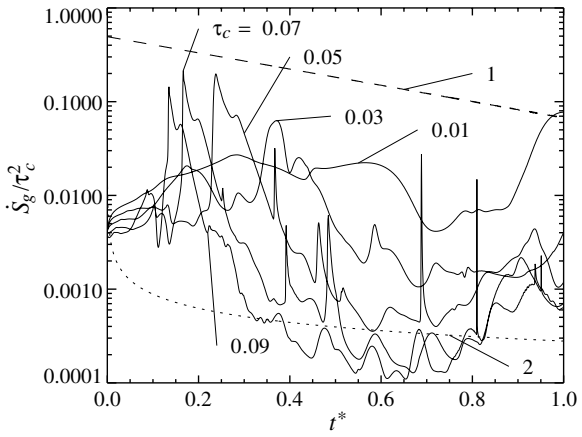

Fig. 11. Unsteady entropy generation rate for $Re = 5 \times 10^4$. Theoretical limits are the fully-mixed and ideally-stratified behaviors, denoted by curves 1 and 2, respectively.

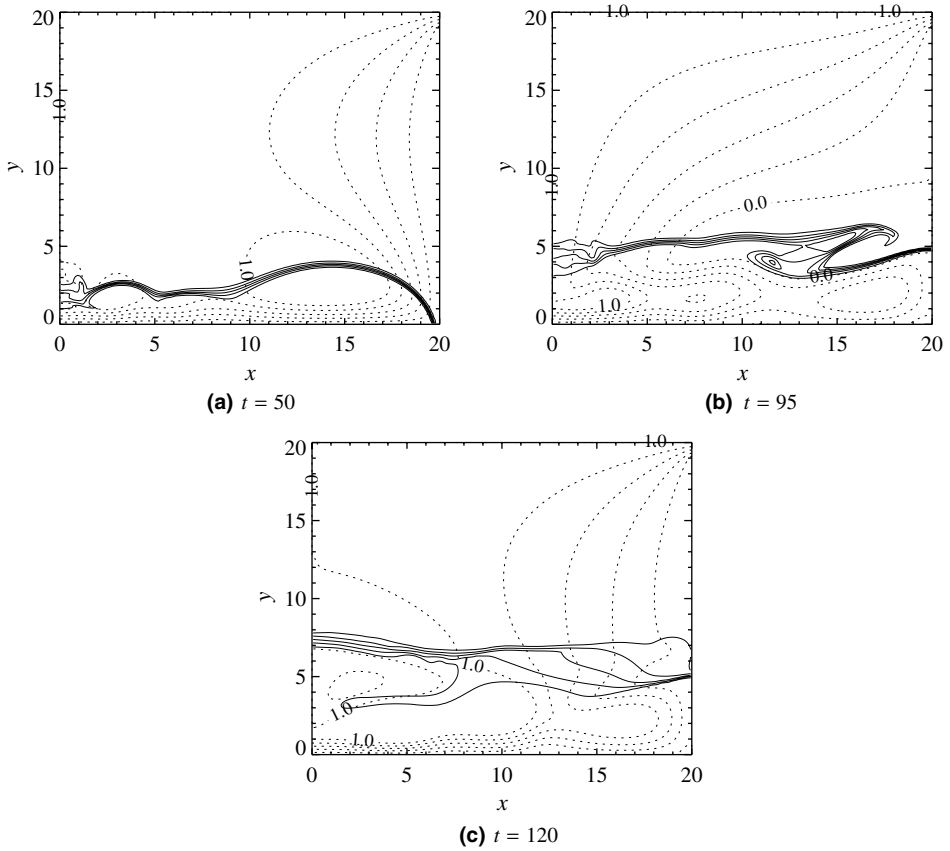

Fig. 12. Isotherm contours ($T = 0.1$, 0.3, 0.5, 0.7, and 0.9) overlayed with instantaneous streamlines ($\Delta\psi = 0.2$) for $Re = 5 \times 10^4$ and $\tau_c = 0.05$ at select times which bracket the peak in the entropy generation rate. The peak in $\dot{S}_g$ occurs at $t = 95$.

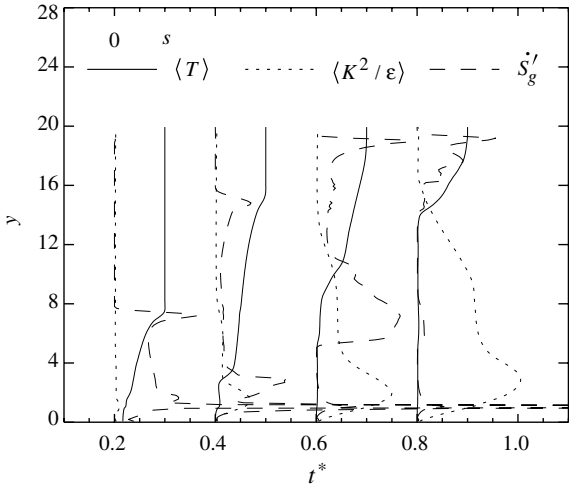

Fig. 13. Vertical profiles of area-averaged temperature, $\langle T\rangle$, ratio of turbulent kinetic energy to dissipation, $\langle K^2/\varepsilon\rangle$, and entropy generation rate, $\dot{S}'_g$ for $Re = 5\times10^4$ and $\tau_c = 0.01$. The scales are $s = 1.0$ for $\langle T\rangle$, $s = 0.25$ for $\langle K^2/\varepsilon\rangle$, and $s = 1.0\times10^{-8}$ for $\dot{S}'_g$.

inertia-dominated domain and $\dot{S}_g/\tau_c^2$ exhibits strong oscillations. The entropy generation rate trends more toward the fully-mixed limit when compared with that in Fig. 7. Throughout the charging process, the $\dot{S}_g/\tau_c^2$ ratio is larger than that of the ideally-stratified limit when $\tau_c \leqslant 0.05$ because of the higher levels of mixing. Some spikes occur at the later stages of the charging process since the gravity currents are bounced by the wall due to the higher inertia.

In Fig. 11, the peak value in $\dot{S}_g/\tau_c^2$ for $\tau_c = 0.05$ occurs at $t^* = 0.2375$, that is, at $t = 95$. Isotherm contours overlayed with instantaneous streamlines for $Re = 5\times10^4$ and $\tau_c = 0.05$ are shown in Fig. 12 for instants both before and after $t = 95$. At $t = 50$, the gravity current has just reached the wall opposite the inlet and the entropy generation is concentrated near the inlet and wall region. At $t = 95$, the gravity current has been turned by the wall opposite the inlet and is moving back toward the inlet as a large amplitude internal wave. At this time, the gradient layer is relatively thin and the entropy generation is focused near the wall opposite the inlet. As the wave-like motion subsides, more fluid is involved in the mixing with the gravity current, causing greater separation in the isotherms. The entropy generation at $t = 120$, for example, is distributed across the whole gradient layer and is less than at $t = 95$.

An overlay of $\langle T\rangle$, $\langle K^2/\varepsilon\rangle$, and $\dot{S}'_g$ is shown in Fig. 13 for the same $Re = 5\times10^4$ and $\tau_c = 0.01$. The gradient layer evident in the averaged vertical temperature profile is larger and exhibits sizable oscillations due to the higher level of inertia and greater mixing effects. The entropy generation, $\dot{S}'_g$, is concentrated in the gradient layer but does not have the regular variation observed in Fig. 9. Instead, it vibrates severely due to the wavy gradient layer. The peak values of $\dot{S}'_g$ appear at the lower and upper edges of the gradient layer. At $t^* = 0.2$, $\dot{S}'_g$ reaches its highest value at the lower edge of the gradient layer. Then, as t^* increases, the peak value of $\dot{S}'_g$ moves toward the upper edge of the gradient layer. The turbulent viscosity increases from zero at the bottom wall to a maximum below the thermocline and then decreases gradually across the gradient layer. Although its impact on the variation of $\dot{S}'_g$ is less pronounced than in the gravity-dominated regime, the turbulent diffusivity is at appreciable levels across much of the gradient layer.

4. Summary and conclusions

Useful volume fraction and internal entropy generation have been utilized to compute the thermodynamic losses for the stably-stratified bottom filling process of a thermal storage vessel. The variations of useful volume fraction and cumulative entropy generation with Reynolds number exhibit two distinct trends corresponding to well-stratified and highly-mixed behaviors. The cumulative entropy generation provides the clearest distinction between these two regimes, termed the gravity-dominated and inertia-dominated regimes, respectively. The transition between the two regimes corresponds to an inlet Froude number of approximately unity. This reinforces earlier guidelines based on visual observations of the initial stages in the filling process (Yoo et al., 1986). In chilled water storage applications for which $\hat{T}_c \simeq 5\,^\circ\mathrm{C}$, cases with inlet Reynolds numbers of up to approximately 2×10^4 and temperature difference ratios of larger than 0.03 remain within the gravity-dominated regime, which provides practical guidelines for the engineering design of these systems.

In the gravity-dominated regime, the useful volume fraction increases linearly with time after an initial adjustment period. The peak in the entropy generation rate occurs when the initial thermocline has been formed across the width of the enclosure at the beginning of the filling process. Recognizing that the peak level of thermal mixing occurs during the initial thermocline formation process provides a theoretical basis for controlling the extent of mixing by changes in the inlet configurations. During most of the charging process, the entropy generation is concentrated primarily within the steep thermal gradient layer in which the turbulent diffusivity is vanishingly small. Although damped by buoyancy within the gradient layer, the turbulent diffusivity does increase rapidly to appreciable levels at the top edge of the gradient layer. Therefore, on the outlet side of the gradient layer, significant levels of entropy generation are produced.

In the inertia-dominated regime, the useful volume fraction increases almost linearly with time and then starts to fall off in later stages of the filling process. The peak in the entropy generation rate occurs after the gravity current has been turned by the wall opposite the inlet. The entropy generation is concentrated in the lower and upper edges of the thermal gradient layer, which is significantly thicker than in the gravity-dominated cases. The turbulent diffusivity does not vanish in the gradient layer and exhibits more gradual variations with vertical position than in the grav-

ity-dominated cases. As a result, the appreciable levels of entropy generation are distributed over a much greater fraction of the enclosure volume.

Acknowledgments

This research was supported in part by the American Society of Heating, Refrigerating and Air Conditioning Engineers (ASHRAE) under the New Investigator Award and the Graduate Grant-in-Aid.

References

Bahnfleth, W.P., Musser, A., 1999. Parametric study of charging inlet diffuser performance in stratified chilled water storage tanks with radial diffusers. Technical report, ASHRAE.

Bejan, A., 1978. Two thermodynamic optima in the design of sensible heat units for energy storage. ASME J. Heat Transfer 100, 708–712.

Bejan, A., 1996. Entropy Generation Minimization. CRC Press.

Benedetti, P., Sciubba, E., 1993. Numerical calculation of the local rate of entropy generation in the flow around a heated finned-tube. ASME HTD 266, 81–91.

Bird, R.B., Stewart, W.E., Lightfoot, E.N., 1960. Transport Phenomena. John Wiley & Sons.

Cabelli, A., 1977. Storage tanks—a numerical experiment. Solar Energy 19, 45–54.

Cai, L., Stewart Jr., W.E., Sohn, C.W., 1993. Turbulent buoyant flows into a 2-d storage tank. Int. J. Heat Mass Transfer 36, 4247–4256.

Chen, Q., 1995. Comparison of different k–ε models for indoor air flow computations. Numer. Heat Transfer, Part B 28, 353–369.

Cheng, C.-H., Huang, W.-H., 1989. Entropy generation and heat transfers via laminar forced-convection channel flows over transverse fins in entrance regions. Appl. Energy 32, 241–267.

Cheng, C.-H., Ma, W.-P., Huang, W.-H., 1994. Numerical predictions of entropy generation for mixed convective flows in a vertical channel with transverse fin array. Int. Commun. Heat Mass Transfer 21, 519–530.

Cole, R.L., Bellinger, F.O., 1982. Natural thermal stratification in tanks, phase 1 final report. Report ANL-82-5, Argonne National Laboratory.

Craft, T.J., Launder, B.E., Suga, K., 1996. Development and application of a cubic eddy-viscosity model of turbulence. Int. J. Heat Fluid Flow 17, 108–115.

Dorgan, C.E., Elleson, J.E., 1994. Design Guide for Cool Thermal Storage. American Society of Heating, Refrigerating, and Air Conditioning Engineers, Inc., Atlanta.

Drost, M.K., White, M.D., 1991. Numerical predictions of local entropy generation in an impinging jet. ASME J. Heat Transfer 113, 823–829.

Guo, K.L., Wu, S.T., 1985. Numerical study of flow and temperature stratification in a liquid storage tank. ASME J. Solar Energy Eng. 107, 15–20.

Hahne, E., Chen, Y., 1998. Numerical study of flow and heat transfer characteristics in hot water stores. Solar Energy 64, 9–18.

Han, S.M., Wu, S.T., Reid, W., Christenson, D.L., 1978. Experimental and numerical study of liquid thermal storage tank models. In: Proceedings of the Annual Meeting, American Section of ISES, pp. 265–270.

Homan, K.O., 1999. Measures of local thermal mixing during filling of stratified thermal storage. In: 33rd National Heat Transfer Conference, ASME, Paper NHTC99-212.

Homan, K.O., 2000. Second law aspects of simplified models for sensible thermal storage. In: Garimella, S., von Spakovsky, M., Somasundaram, S. (Eds.), Proceedings of the ASME Advanced Energy Systems Division, vol. 40, pp. 413–422.

Homan, K.O., 2003. Internal entropy generation limits for direct sensible thermal storage. ASME J. Energy Resour. Technol. 125, 85–93.

Homan, K.O., Soo, S.L., 1998. Laminar flow efficiency of stratified chilled-water storage tanks. Int. J. Heat Fluid Flow 19, 69–78.

Krane, R.J., 1987. A second law analysis of the optimum design and operation of thermal energy storage systems. Int. J. Heat Mass Transfer 30, 43–57.

Krane, R.J., Krane, M.J.M., 1992a. The optimum design of stratified thermal energy storage systems—Part I: Development of the basic analytical model. J. Energy Resour. Technol. 114, 197–203.

Krane, R.J., Krane, M.J.M., 1992b. The optimum design of stratified thermal energy storage systems—Part II: Completion of the analytical model, presentation and interpretation of the results. ASME J. Energy Resour. Technol. 114, 204–208.

Lage, J.L., Bejan, A., Anderson, R., 1991. Efficiency of transient contaminant removal from a slot ventilated enclosure. Int. J. Heat Mass Transfer 34, 2603–2615.

Lage, J.L., Bejan, A., Anderson, R., 1992. Removal of contaminant generated by a discrete source in a slot ventilated enclosure. Int. J. Heat Mass Transfer 35, 1169–1180.

Leonard, B.P., 1979. A stable and accurate convective modeling procedure based on quadratic upstream interpolation. Comput. Methods Appl. Mech. Eng. 19, 59–98.

Mavros, P., Belessiotis, V., Haralambopoulos, P., 1994. Stratified energy storage vessels: characterization of performance and modeling of mixing behavior. Solar Energy 52, 327–336.

Mo, Y., Miyatake, O., 1996. Numerical analysis of the transient turbulent flow field in a thermally stratified thermal storage water tank. Numer. Heat Transfer, Part A 30, 649–667.

Moran, M.J., Keyhani, V., 1982. Second law analysis of thermal energy storage systems. In: Proceedings of the Seventh International Heat Transfer Conference, vol. 6, pp. 473–478.

Nakayama, A., 1995. PC-Aided Numerical Heat Transfer and Convective Flow. CRC Press.

Oppel, F.J., Ghajar, A.J., Moretti, P.M., 1986. A numerical and experimental study of stratified thermal storage. ASHRAE Trans. 92, 293–309.

Patankar, S.V., 1980. Numerical Heat Transfer and Fluid Flow. McGraw-Hill, New York.

Rodi, W., 1979. Turbulence models and their application in hydraulics. International Association for Hydraulic Research.

Spall, R.E., 1998. A numerical study of transient mixed convection in cylindrical thermal storage tanks. Int. J. Heat Mass Transfer 41, 2003–2011.

Speziale, C.G., 1987. On nonlinear k–l and k–ε models of turbulence. J. Fluid Mech. 178, 459–475.

Truman, C.R., Wildin, M.W., 1989. Finite difference model for heat transfer in a stratified thermal storage tank with throughflow. In: ASME/AIChE Nat. Heat Transfer Conf., ASME HTD, vol. 110, pp. 45–55.

White, F.M., 1991. Viscous Fluid Flow. McGraw-Hill, New York.

Yoo, J., Wildin, M.W., Truman, C.R., 1986. Initial formation of a thermocline in stratified thermal storage tanks. ASHRAE Trans. 92, 280–292.

Zurigat, Y.H., Liche, P.R., Ghajar, A.J., 1991. Influence of inlet geometry on mixing in thermocline thermal energy storage. Int. J. Heat Mass Transfer 34, 115–125.